AIAA 2001-3584

Modeling the Gas Dynamics Environment in as Subscale Solid Rocket Test Motor

Andrew M. Eaton, Mark E. Ewing and Kirk M. Bailey

37th AIAA/ASME/SAE/ASEE
Joint Propulsion Conference and Exhibit
July 8-11, 2001
Salt Palace Convention Center
Salt Lake City, Utah

MODELING THE GAS DYNAMICS ENVIRONMENT IN A SUBSCALE SOLID ROCKET TEST MOTOR

Andrew M. Eaton,* Mark E. Ewing† and Kirk M. Bailey‡
ATK Thiokol Propulsion Corp.
Brigham City, Utah

ABSTRACT

Subscale test motors are often used for the evaluation of solid rocket motor component materials such as internal insulation. These motors are useful for characterizing insulation performance behavior, screening insulation material candidates and obtaining material thermal and ablative property design data. One of the primary challenges associated with using subscale motors however, is the uncertainty involved when extrapolating the results to full-scale motor conditions. These uncertainties are related to differences in such phenomena as turbulent flow behavior and boundary layer development, propellant particle interactions with the wall, insulation off-gas mixing and thermochemial reactions with the bulk flow, radiation levels, material response to the local environment, and other anomalous flow conditions. In addition to the need for better understanding of physical mechanisms, there is also a need to better understand how to best simulate these phenomena using numerical modeling approaches such as computational fluid dynamics (CFD).

To better understand and model interactions between major phenomena in a subscale test motor, a numerical study of the internal flow environment of a representative motor was performed. Simulation of the environment included not only gas dynamics, but two-phase flow modeling of entrained alumina particles like those found in an aluminized propellant, and off-gassing from wall surfaces similar to an ablating insulation material.

This work represents a starting point for establishing the internal environment of a subscale test motor using comprehensive modeling techniques, and lays the groundwork for improving the understanding of the applicability of subscale test data to full-scale motors. It was found that grid resolution, and inclusion of phenomena in addition to gas dynamics, such as two-phase and multi-component gas composition are all important factors that can effect the overall flow field predictions.

INTRODUCTION

Subscale test motors are often used for the evaluation of solid rocket motor component materials such as internal insulation. An example of one such motor is referred to as a Seventy Pound Charge or 'SPC' motor, the name originating from the propellant weight originally used in an early design of the motor. These motors are useful for characterizing insulation performance behavior, screening insulation material candidates and obtaining material thermal and ablative property design data.

One of the primary challenges associated with using subscale motors is the uncertainty involved when extrapolating the results to full-scale motor conditions. For example, insulation erosion in the SPC char motor may be quite different than observed in a full-scale motor for what were thought to be similar Mach numbers. The uncertainties are typically the result of an inadequate understanding of the local aerothermal environment of the subscale motor compared with the full-scale. These uncertainties can be attributed to any, or a combination of any of the following:

1) Turbulent flow behavior and boundary layer development may be much different.
2) Metallized propellant particle interactions with the wall may not be representative of particle interactions in certain regions of full-scale motors.
3) Pyrolysis gas products leaving the surface of the insulator may have higher relative concentration levels that could lead to differences in material ablation behavior.
4) Radiation levels may be lower than those in full-scale motors due to the small scale and associated optical thickness.
5) Non-uniform erosion behavior in multiple samples may result in anomalous flow conditions.

* Supervisor, Gas Dynamics Section
† Senior Principal Engineer, Heat Transfer Section
‡ Senior Principal Engineer, Insulation Section

6) Uncertainties in the how the material response is related to the local environment.

In addition to the need for understanding these physical mechanisms, there is also a need to better understand how to best simulate these phenomena using numerical modeling approaches such as computational fluid dynamics (CFD). Of particular interest are the use of 'comprehensive' codes that employ fully-coupled solutions of the gas dynamics with two-phase flow and multi-component gases. CFD-related tools can provide insights into the interplay of the various mechanisms of interest and also serve as a scaling tool for comparing small motor and large motor environments if the appropriate modeling approaches can be identified. These approaches are related to areas such as turbulence modeling and the associated wall-boundary condition approach, and how fine the computational grid must be to accurately capture the flow details of interest.

To help address these issues, a numerical study of the internal flow environment of an SPC motor was performed. The objective of this study was to assess the sensitivity of the internal aerothermal environment predictions of the SPC test motor to grid fineness and associated wall boundary condition approach. Simulation of the environment included not only gas dynamics, but two-phase flow modeling of entrained alumina particles like those found in an aluminized propellant, and off-gassing from wall surfaces similar to an ablating insulation material

DESCRIPTION OF CFD SIMULATIONS

To achieve the objectives of this study, a series of SPC flow predictions were done for both a relatively coarse and a finely meshed computational grid. Given the two grids, three different kinds of flow situations were considered: assuming all the propellant combustion products flow as a single-phase gas flow, assuming a two-phase mix of propellant gas combustion products and entrained alumina particles, and single-phase gas flow with two gaseous components (propellant combustion products and insulation charring-ablation off-gas).

Geometry

A sketch of the geometry of the SPC motor considered in this study is shown in Fig. 1. When testing insulation materials in this motor, performance can be characterized over a wide range of operating conditions by varying the bore diameter in the three flow regions of the motor designated as the low, medium and high velocity sections. In these regions, flow diameters can vary from as large as 20 to as small as 3.2-cm, with corresponding Mach numbers ranging from 0.0027 to 0.08 and gas velocities ranging from 3.5 to 110-m/sec respectively. A typical test motor pressure can be as high as 5.5-6.5-MPa.

General Assumptions and Operating Conditions

In modeling the SPC internal flow field, all of the predictions of the internal environment were made with the commercially available Fluent® CFD code, and the following general assumptions and operating conditions were used:

- Axisymmetric, compressible flow.
- Two-equation RNG-k-ε turbulence model, which has demonstrated improved predictions compared with the standard k-ε model [1,2].
- Steady-state flow.
- Constant wall boundary temperature (2500K) for the areas of the motor corresponding to insulation samples, adiabatic walls elsewhere.
- Propellant gas properties with molecular weight = 28.44, dynamic viscosity = 9.65x10-5 kg/m-s, Specific heat = 2000 J/kg and thermal conductivity = 0.38 W/m-K.
- Total propellant mass flow rate of 0.49 kg/s, at a total pressure of 6.2 MPa and a total temperature of 3400K.

Gridding and turbulence modeling

Given the general operating conditions and assumptions, the primary objective of this study was to assess the sensitivity of the flow field predictions to grid resolution. Of particular interest was the wall heat transfer. In turbulent flow modeling however, the creation of the grid is closely coupled with the choice of the wall boundary condition approach. A review of turbulent flow models and the options available for defining wall boundary conditions has been performed by several investigators, such as Wilcox[3], Pope[4] and Eaton, et al[5]. Based on these reviews, two cases were chosen as representative to assess the effects of grid resolution and the related wall boundary condition approach on the wall heat transfer:

1. A relatively coarse grid (10,000 cells) and a wall function boundary condition.
2. A relatively fine grid (100,000 cells) and a two-layer zonal boundary condition.

Coarse grid case. Launder and Spalding [6,7] first proposed the standard wall function boundary condition for CFD-related predictions using a two-equation turbulence model. This boundary condition is based on the assumption that a universal velocity and temperature profile exists between the wall node center of the fluid cell adjacent to the wall. The velocity and temperature profiles can be described in non-dimensional coordinates as

$$U^* = \frac{1}{\kappa}\ln(Ey^*)$$

$$T^* = \mathrm{Pr}_t(U^* + P)$$

where

$$U^* \equiv \frac{UC_\mu^{1/4}k^{1/2}}{\tau_w/\rho}$$

$$T^* \equiv \frac{(T_w - T)C_p C_\mu^{1/4}k^{1/2}\rho}{\dot{q}''}$$

and

$$y^* \equiv \frac{C_\mu^{1/4}k^{1/2}y}{\nu}$$

U and T are the velocity and temperature at the node center of the fluid cell adjacent to the wall, y is the distance from the wall to the node center, and k is the turbulent kinetic energy. C_μ, κ, and E are empirical constants, Cp, ρ, and ν are the local fluid properties of specific heat, density and kinematic viscosity respectively, and τ_w is the local wall shear stress. These expressions for U^*, T^*, and y^* are the same as expressions for universal log-law in terms of U^+, T^+, and y^+ described in references such as Kays and Crawford[8], given the relationships

$$U^* = aU^+$$

$$T^* = aT^+$$

$$y^* = ay^+$$

where a is defined by the ratio

$$a = \frac{C_\mu^{1/4}k^{1/2}}{\sqrt{\tau_w/\rho}}$$

The ratio a is a measure of the development of the boundary layer. In a developing boundary layer, it is less than 1, in a fully-developed boundary layer it is about equal to 1, and boundary layers with high free-stream turbulence, such as a wall jet, it is greater than 1. Given a cell velocity, the log-wall relationships relates the local shear stress imposed by the wall on the flow with the neighboring cell velocity.

When creating a grid for a prediction that will employ a wall function boundary condition, the main controlling parameter driving the grid resolution is the magnitude of y^* for the fluid cell adjacent to the wall. To keep this wall function in its range of applicability, the y* value should ideally be in the range of 30-100. Following this criterion for the SPC motor resulted in a grid with 10,000 cells.

Fine grid case. For the fine grid case, the two-layer zonal boundary condition presented by Rodi[9], Chen and Patel[10] and Kim and Choudhury[11] was employed, which has been shown to be more robust and provide better performance than alternative low-Reynolds k-ε turbulence models. In contrast with the wall function approach, the two-layer zonal boundary condition approach makes no assumption about the velocity profile, but calculates it directly based on the local grid spacing. It does this by dividing the flow field into two main parts, a region along the wall dominated by viscous effects, and a region away from the wall corresponding to fully-turbulent flow. In the near-wall region, a one-equation turbulence model is employed, and the high-Reynolds number RNG-model is used in the fully-turbulent region. This approach therefore requires grid resolution that extends into the viscous sublayer of the flow, which corresponds to y+ values in the neighborhood of 1. Given this kind of grid resolution, the two-layer model accounts for the changes in turbulent kinetic energy and dissipation in the near-wall region of the flow field. For the SPC motor, following the requirements for the two-layer wall boundary condition resulted in a grid with about 120,000 cells.

Particle transport

In additional to the single-phase gas flow cases, for the two computational grids described above, fully-coupled two-phase predictions were made to characterize the particle transport. The particle size distribution and loading were similar to those described by Whitesides et al[12] for RSRM propellant. The size distribution was divided into 8 separate sizes with a minimum diameter of 10 microns, a maximum diameter of 600 microns, a mean diameter of 93.7 microns and a spread factor of 1.157. For the particles, the density was assumed to be 100 kg/m3, the specific heat 1760 J/kg and a conductivity of 10.5 W/m-K.

The loading of the particles corresponded to about 8% of the total mass flow rate of the propellant (0.0395 kg/s), which is representative of the amount of alumina particle in the propellant gas with diameters equal to or greater than about 10 microns.

Insulation Off-gassing

In addition to the single and two-phase calculations, for the two computational grids described above, the off-gassing of the ablating insulators into the propellant gas was modeled as an in-flow boundary condition. These were modeled as gas-only flows, but the insulation off-gas representing the charring/ablation products was modeled with one composition, and the propellant gas as another composition. The composition of the off-gas was assumed to correspond to the elemental composition of the insulation, which is a mix of carbon, ethylene, propylene, and neoprene. This

mixture was calculated to have an equivalent molecular weight of 26.38. No reactions were assumed and the mixing was driven by diffusion and turbulence transport. The mass flow rates assumed for each of the sections was base on typical insulation erosion rates, which are as follows:

- Low velocity section = 0.0054 kg/s
- Medium velocity section = 0.0039 kg/s
- High velocity section = 0.0073 kg/s

RESULTS OF THE PREDICTIONS

The results of the predictions for all the cases are summarized in Figures 2-10. While the full-motor was analyzed, figures with contour images have been magnified in areas where the insulation sections would be located.

Figure 2 is a comparison of velocity and stream function predictions for the single-phase gas flow cases. As seen in these figures, very different flow fields are predicted for the two cases. The fine grid case predicts greater mass flow along the walls than in the coarse grid case. There is a corresponding higher heat flux rate in the fine grid case, which is evident in the lower gas temperature for the fine grid case shown in the comparisons in Figure 3. The values for the wall heat flux are between the two cases are compared in Figure 4.

Figure 5 is a comparison of velocity and temperature for the two-phase flow cases. In these predictions, the differences between the coarse and fine grid predictions are not as great as the single-phase gas predictions. One of the reasons for this is shown in Figure 6, which compares coarse and fine grid particle concentrations. Both predict that the particles entering the medium and high velocity section of the motor tend to concentrate along the centerline of the motor rather than staying in a uniform distribution. As a result the differences in gas temperature, shown in Figure 5, and the heat flux, shown in Figure 4, are also not as great as in the single-phase cases. There is enough of a difference in the flow field predictions however, to alter the level of particle concentrations along the wall. These comparisons are shown in Figure 7. Much higher particle concentrations are predicted for the fine grid case than the coarse grid case.

Figure 8 compares contour images of the insulation off-gas fraction for the two-component gas flow predictions. The gas fraction values along the wall are shown in Figure 9. These comparisons show that the grid resolution does not significantly affect the prediction of off-gas fraction along the wall. In relating this parameter to the corresponding effect on insulation erosion, it is useful to calculate how the insulation off-gas fraction affects the value of β, which is defined by McDonald and Headman[13] as

$$\beta = \frac{MW_e\left(X_{H_2O} + X_{CO_2} + 2X_{O_2} + X_O + X_{OH}\right)}{(MW_e)(1 - X_{Al_2O_3}) - X_{Al_2O_3}(MW_{Al_2O_3})}$$

where MW_e is the molecular weight of the gas at the edge of the boundary layer, $MW_{Al_2O_3}$ is the molecular weight of the alumina in the entrained particles, and X_j is the mole fraction of the species j. β can be shown to be the ratio of char oxidation rate to the rate at which oxidizing species from the boundary layer edge can diffuse to the wall. The presence of upstream off-gas can therefore dilute the oxidizing species and attenuate char oxidation. To determine the relationship between off-gas fraction and β, a series of mixing calculations were made with the NASA-Lewis code. This relationship is shown in Figure 10. As an example of the effect of off-gas, a value of 0.04, which is representative of the value in the medium and high-velocity sections of the char motor, β is reduced from 0.1 to 0.04, which would be a 40% reduction in the char rate. The mixing of the off-gas with the propellant can therefore have a noticeable affect on downstream erosion.

CONCLUSIONS

This work is the starting point for establishing the internal environment of a subscale test motor, and lays the groundwork for improving the understanding of the applicability of subscale test data to full-scale motors. The results may also give insights into the appropriate design of improved subscale testbeds, and provide valuable information for improved modeling techniques for internal insulation.

Grid resolution and the related wall boundary condition approach used in the simulations was demonstrated to be an important factor in prediction results. If we follow the standard assumption that increasing grid resolution increases the accuracy of the prediction, then the fine grid predictions best represent the flow field and suggest that wall function approaches may not provide the needed accuracy. The comparison with the two-phase simulations indicate however, that the affects of grid spacing and wall boundary condition are attenuated by the addition of a the discrete phase.

Coupling of the gas dynamics with entrained particles in the two-phase predictions was also found to have an major effect on the flow field predictions, although the difference was not as great for the coarse grid case as

the fine grid case. The change in particle concentrations when flowing into regions where there are significant changes in geometry, like the transition from the low-velocity to high velocity sections of the motor can have a dramatic effects on the resulting overall gas flow distribution. These results suggest the need for two-phase flow predictions to accurately characterize the dynamics of the flow field.

From the multi-component predictions, it can be concluded that the local environment needs to be properly characterized in order to fully understand local component behavior. For example, upstream insulation erosion has the potential to affect downstream erosion because of changes introduced in the local environment.

As an overall conslusion from this study, there is a definite need to apply more comprehensive modeling approaches in studying the internal flow of solid rocket motors. This need is as great in obtaining accurate predictions as the need for adequate grid resolution. The changes in flow field predictions that result when more complex physics is included in the prediction have underscored this need, as well as illustrating how the differences in local environment in comprehensive model predictions may have significant effects on the local material response.

REFERENCES

1. Yakhot, V. and Orzsag, S.A. Renormalization group analysis of turbulence: I. Basic Theory. J. Scientific Computing. 1(1):1, 1986.
2. Choi, D., J.S. Sabnis and T.J. Barber. Application of an RNG k-epsilon turbulence model to compressible turbulent shear layers. AIAA 94-0188.
3. Wilcox, D.C. Turbulence modeling for CFD. La Canada, CA: DCW Industries, Inc., 1998.
4. Pope, S.B. Turbulent Flows. Cambridge. Cambridge University Press. 2000.
5. Eaton, A.M., Smoot, L.D., Hill, S.C. and Eatough, C.N. Components, formulations, solutions, evaluation, and application of comprehensive combustion models. *Prog. Energy Combustion Science. 1999*; 25:387.
6. Launder, B.E. and Spalding, D.B. Lectures in mathematical models of turbulence. New York: Academic Press, 1972.
7. Launder, B.E. and Spalding, D.B. The numerical computation of turbulent flows. *Computer Methods in Applied Mechanics and Engineering*, 3:269, 1974.
8. Kays, W.M. and Crawford, M.E. Convective Heat and Mass Transfer. New York, McGraw Hill, 1980.
9. Rodi, W. Experience with 2-layer models combining the k-e model with 1-equation model near the wall. AIAA Paper 91-0216. 1991.
10. Chen, H.C. and Patel, V.C. Near-wall turbulence models for complex flows including separation. *AIAA J. 26(6):641*, 1988.
11. Kim, S., and Choudhury, D. Computations of complex turbulent flows and heat transfer using two-layer based wall functions. ASME HTD-Vol. 311. 1995 National Heat Transfer Conference. 9. 169. 1995.
12. Whitesides, R.H. Dill, R.A. and Purinton, D.C. Application of two-phase CFD analysis to the evaluation of asbestos-free insulation in the RSRM. AIAA-97-2861. 1991.
13. McDonald, A.J. and Hedman, P.O. Erosion of graphite in solid-pro0pellant combustion gases and

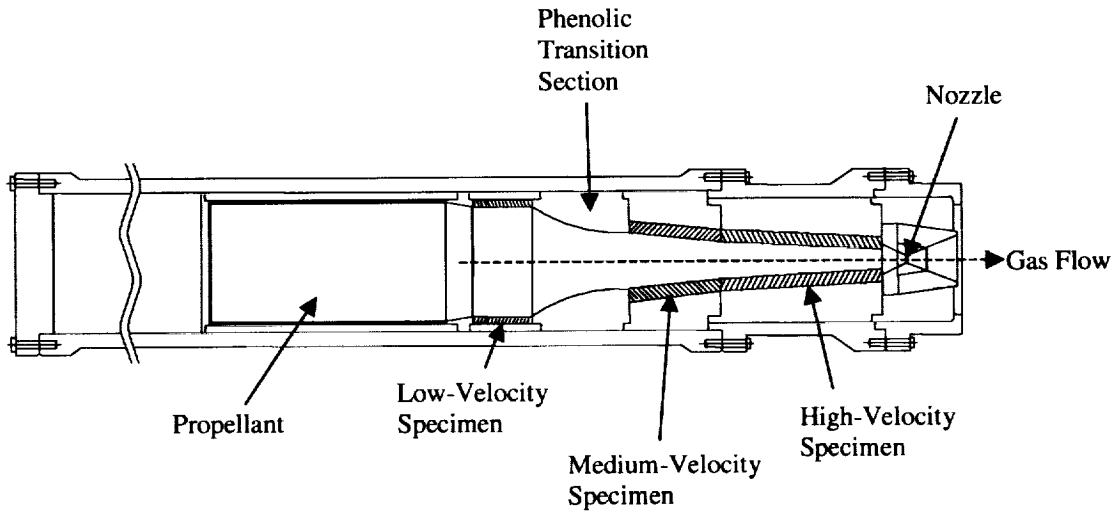

Figure 1. Sketch of the SPC char motor

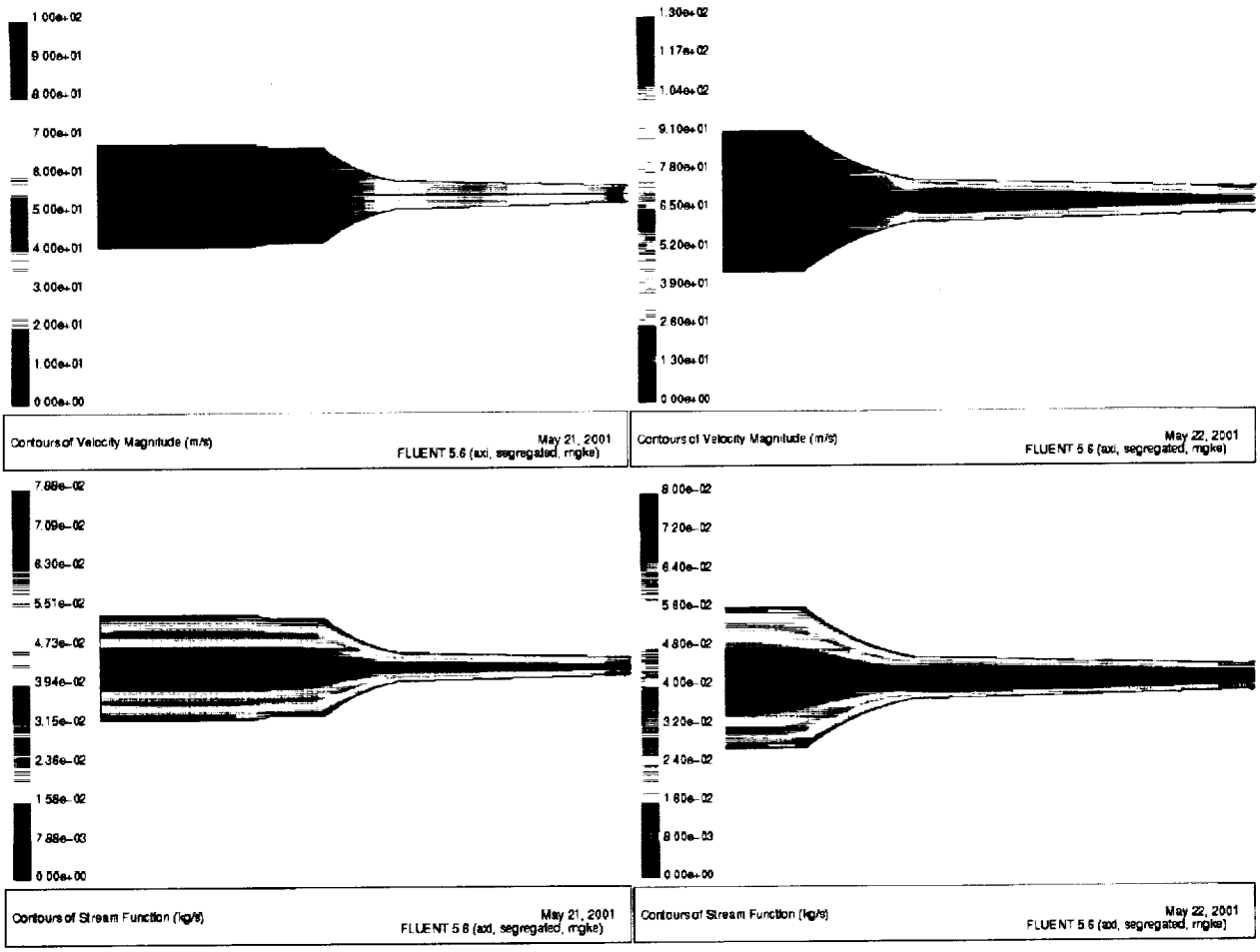

a. Coarse grid with wall function b. Fine grid with two-layer zonal

Figure 2. Comparison of single-phase gas velocity magnitude and stream function.

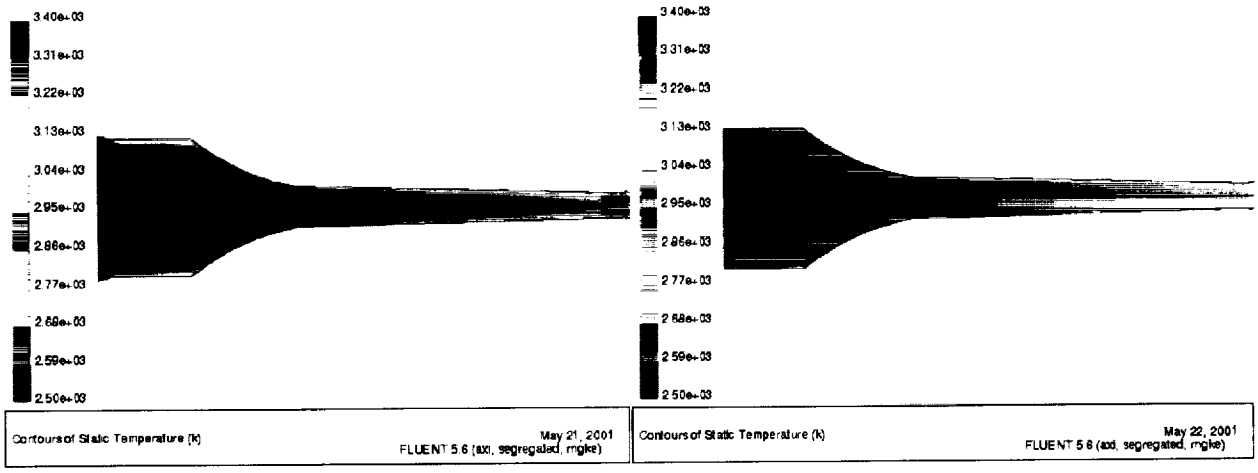

a. Coarse grid b. Fine grid

Figure 3. Comparison of single-phase gas temperatures.

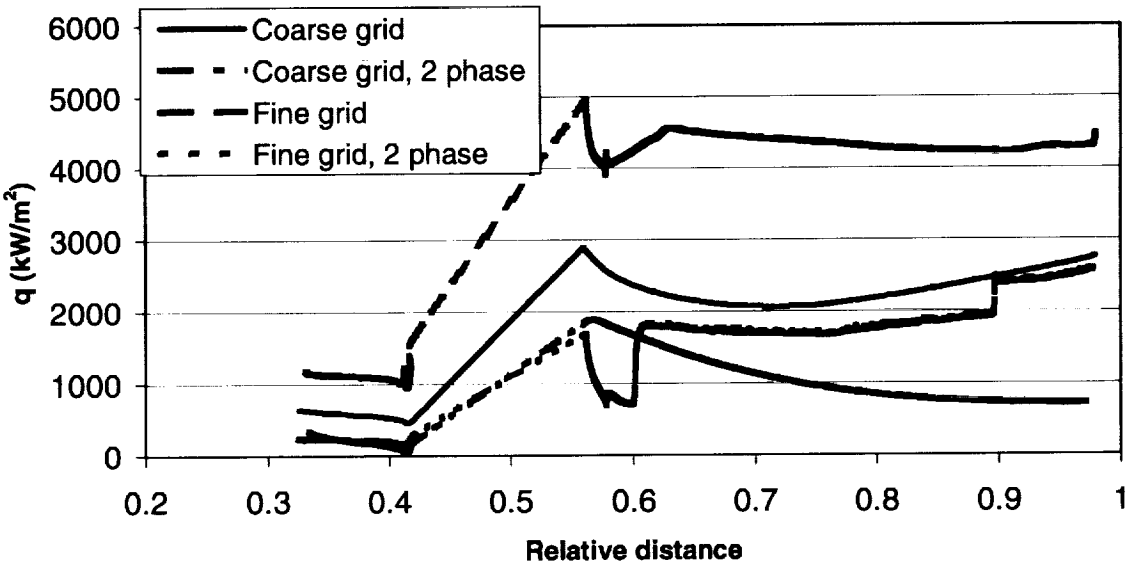

Figure 4. Predicted wall heat flux for the single and two-phase flow predictions.

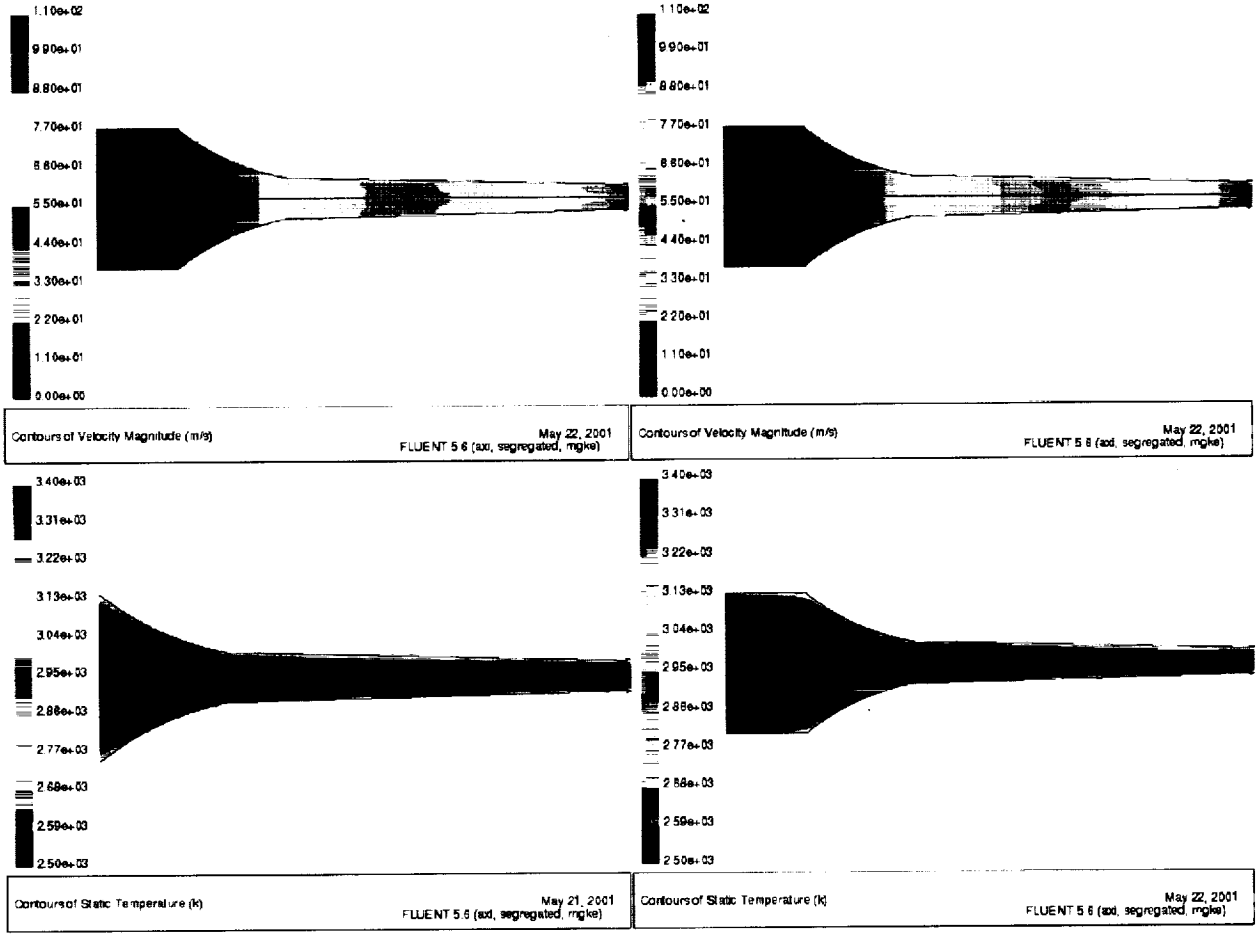

a. Coarse grid b. Fine grid

Figure 5. Comparison of velocity and temperature for the 2-phase flow predictions.

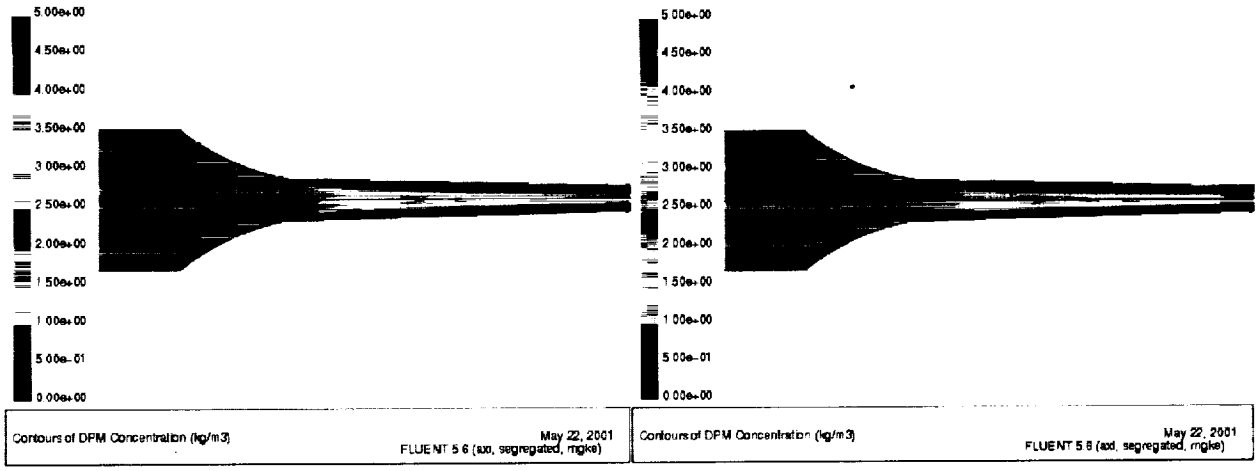

a. Coarse grid b. Fine grid

Figure 6. Comparison of particle concentrations

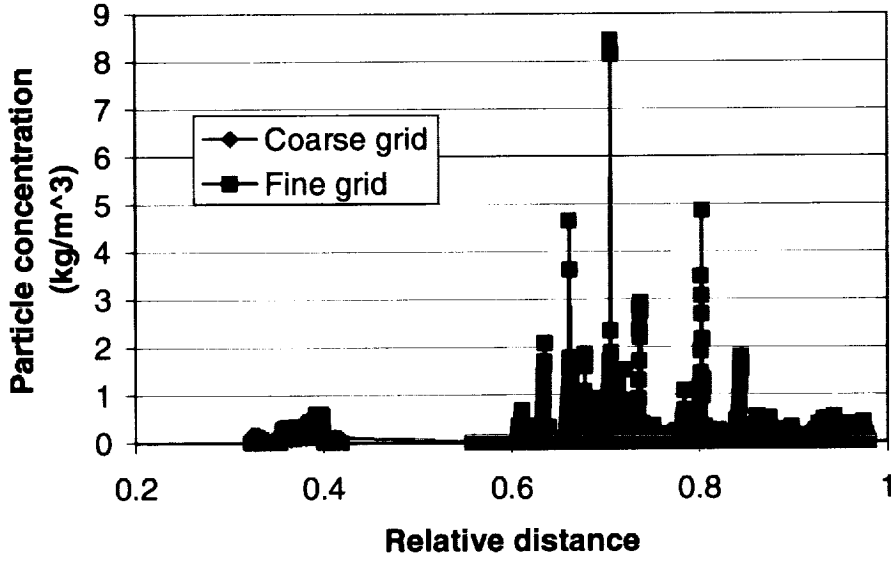

Figure 7. Comparison of particle concentrations along the wall.

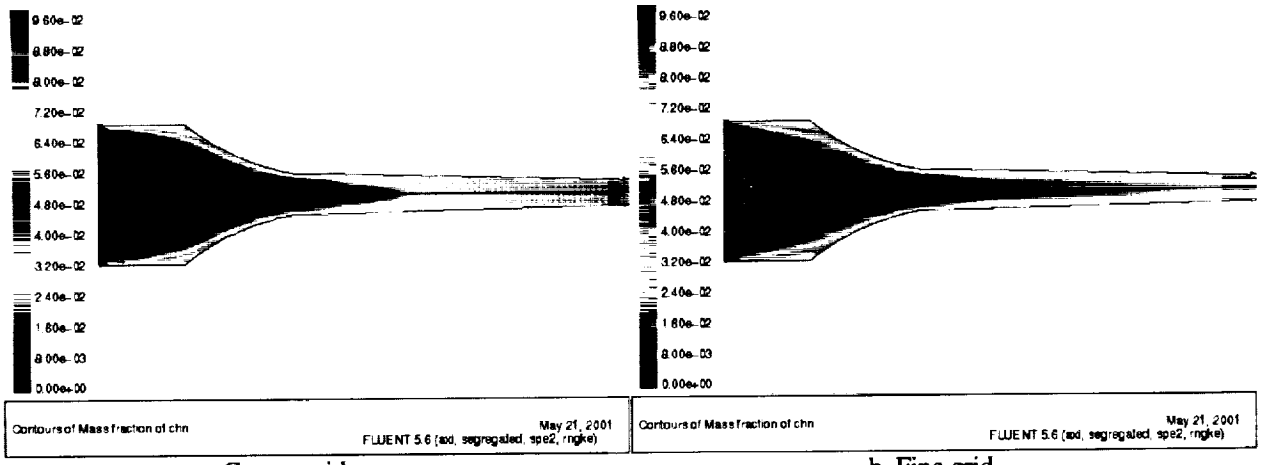

a. Coarse grid b. Fine grid

Figure 8. Comparisons of insulation off-gas fraction.

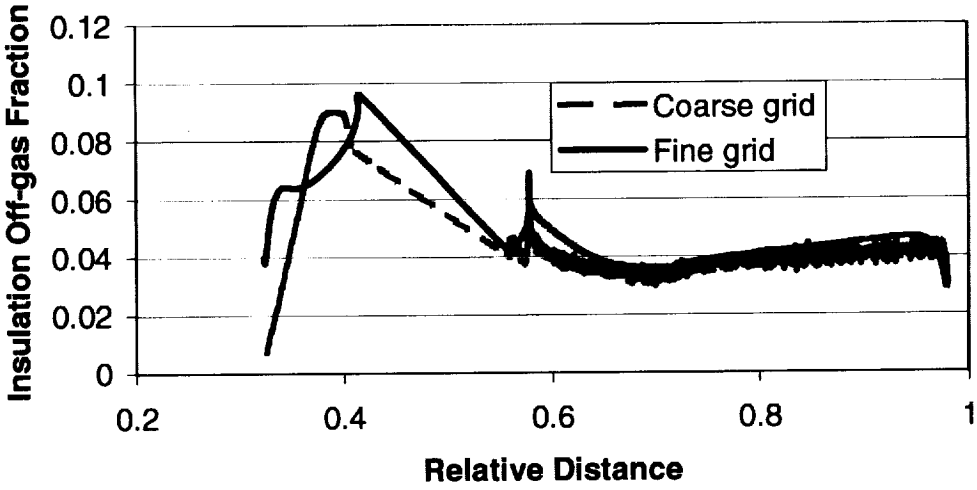

Figure 9. Comparison of insulation off-gas fraction along the wall.

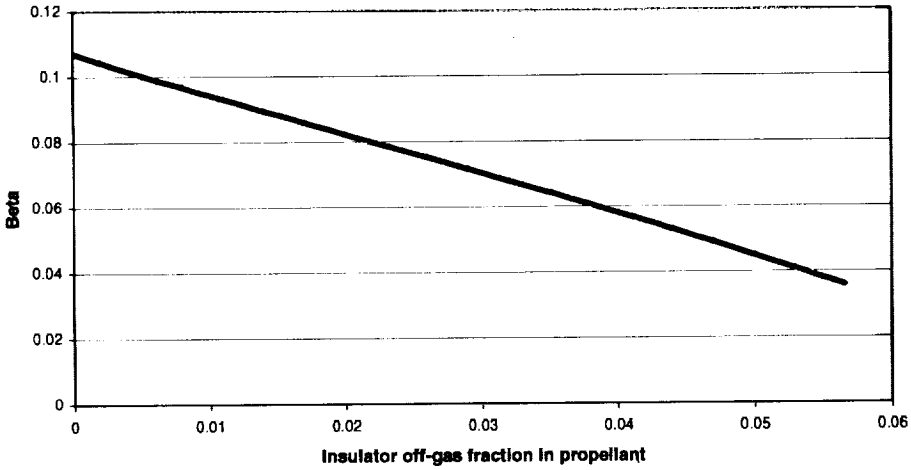

Figure 10. Beta as a function of off-gas fraction